

<https://doi.org/10.1038/s43247-025-02446-3>

The Gulf Stream moved northward at the end of the Little Ice Age

Check for updates

Edward C. G. Forman^{1,2}✉, James U. L. Baldini¹, Robert A. Jamieson³, Franziska A. Lechleitner⁴, Izabela W. Walczak⁵, Dan C. Nita^{6,7}, Struan R. Smith⁸, David A. Richards⁶, Lisa M. Baldini⁹, Cameron McIntyre^{10,11}, Wolfgang Müller¹² & Andrew J. Peters¹³

The Gulf Stream forms part of the upper-ocean limb of the Atlantic Meridional Overturning Circulation, playing an essential role in redistributing heat northward and greatly influencing regional climates in the North Atlantic. Understanding Gulf Stream path and strength variability on pre-instrumental timescales is vital to contextualise its proposed present-day weakening and to better appreciate its sensitivity to external forcing. Here we present a 564 year-long monthly resolved terrestrial palaeo-oceanographic temperature record derived from a Bermudan stalagmite, spanning 1449 to 2013 in the Common Era. Our reconstruction suggests that the Gulf Stream migrated northward as the Little Ice Age abated, after a combination of reduced Gulf Stream transport, enhanced Labrador Current and Deep Western Boundary Current transport, and an extended negative North Atlantic Oscillation phase had likely forced its path southward.

The system of ocean currents collectively known as the Atlantic Meridional Overturning Circulation (AMOC) are a major driver of climate variability. The AMOC is a highly non-linear system, and some climate models suggest that it will cross a tipping point this century due to additional external forcing from increasing greenhouse gas concentrations^{1,2}. A substantial AMOC slowdown would have serious ramifications for regional climates, such as up to ~15 °C mean annual temperature reductions in Northwest Europe³. Thus, understanding its response to climate forcing is critical. One key component of the AMOC is the Gulf Stream (GS), which transports warm water from the Gulf of Mexico northward towards Northwest Europe (Fig. 1). Due in part to the GS, winter surface air temperatures in western Europe are up to 10 °C higher than the zonal mean at comparable latitudes⁴. GS path and AMOC strength are intrinsically linked. A weaker AMOC reduces the Deep Western Boundary Current (DWBC), weakens the northern recirculation gyre, and shifts the GS separation point northward⁵. Anthropogenic warming has reduced AMOC strength to perhaps its weakest state over the past millennium, inducing a northward migration of the Gulf Stream North Wall^{6,7}. Temperature records from the Gulf of Maine have traced the effects of GS path migration over the last 100 years⁸, with

northward movement raising regional sea surface temperatures (SSTs). However, on pre-instrumental timescales that are critical for understanding sensitivity to global temperature change, precise GS position remains elusive.

The Little Ice Age (LIA; 1300–1850 CE) represents a key time interval for understanding how GS positioning and dynamics respond to climate change because it was characterised by extended Northern Hemisphere (NH) cold intervals. Proxy evidence suggests the LIA featured a GS that was approximately 10% weaker and positioned further south, likely due to a stronger Labrador Current (LC) and enhanced recirculation gyre^{9–11}. The lack of instrumental records from the LIA means that palaeoclimate reconstructions are crucial for inferring GS state and position.

Stalagmites are increasingly providing important constraints on the interpretation of palaeoclimates, particularly due to their propensity to provide accurate and precise chronologies and potential for continuous, high-resolution records, in some cases at sub-monthly timescales. Strong environmental seasonality can result in visible or geochemical laminations offering high-precision chronological control, complementing any radiometric (e.g., U–Th or ¹⁴C) determinations (e.g., refs. 12,13). Magnesium

¹Department of Earth Sciences, University of Durham, Durham, UK. ²School of Geography and Environmental Science, University of Southampton, Southampton, UK. ³Earth Surface Science Institute, School of Earth and Environment, University of Leeds, Leeds, UK. ⁴Department of Chemistry, Biochemistry and Pharmaceutical Sciences, and Oeschger Centre for Climate Change Research, University of Bern, Bern, Switzerland. ⁵Durham Centre for Academic Development, University of Durham, Durham, UK. ⁶School of Geographical Sciences, University of Bristol, Bristol, UK. ⁷Institute for Research, Development and Innovation in Applied Natural Sciences, Babes-Bolyai University, Cluj-Napoca, Romania. ⁸Natural History Museum, Bermuda Aquarium Museum and Zoo, Flatts Village, Bermuda. ⁹School of Health & Life Sciences, Teesside University, Middlesbrough, UK. ¹⁰Laboratory of Ion Beam Physics, ETH Zürich, Zürich, Switzerland. ¹¹AMS Laboratory, Scottish Universities Environmental Research Centre (SUERC), East Kilbride, UK. ¹²Institute of Geosciences, Goethe University Frankfurt, Frankfurt am Main, Germany. ¹³ASU Bermuda Institute of Ocean Sciences, St. George's, Bermuda. ✉e-mail: E.Forman@soton.ac.uk

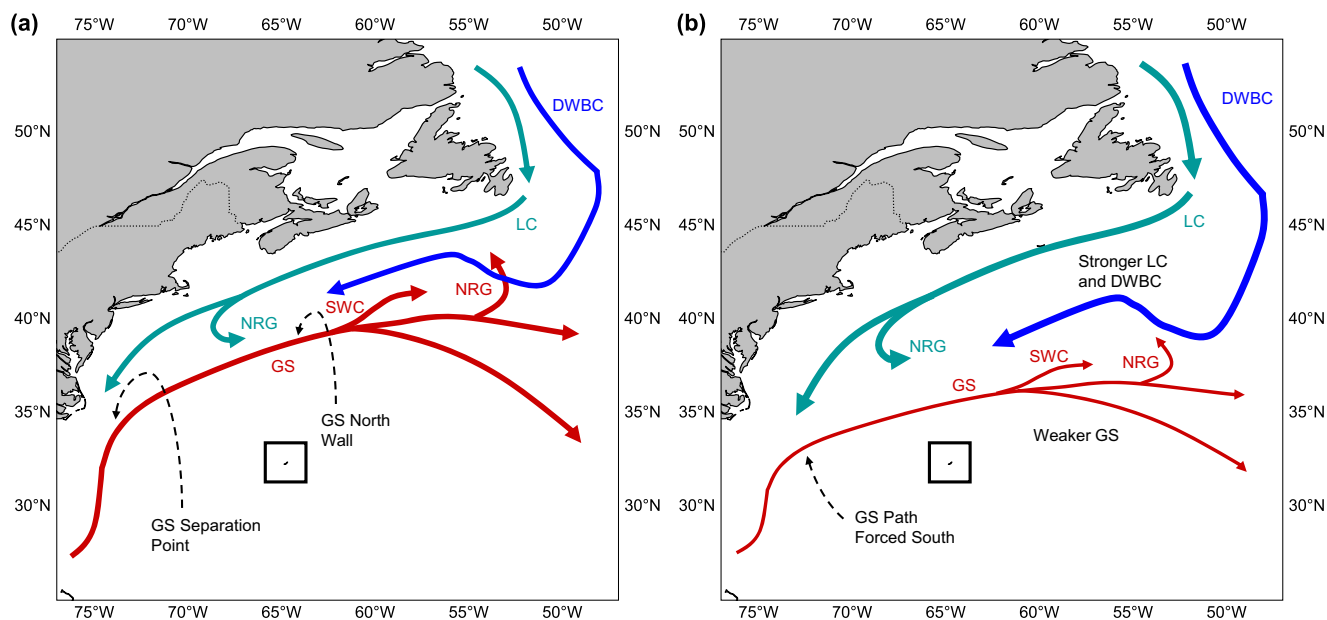


Fig. 1 | Schematic of relevant ocean currents in the North Atlantic Ocean.

a Idealised modern day ocean currents (modified from ref. 88). The GS North Wall describes the northern extent of the GS and is defined by the strong temperature front. The point at which the path of the GS diverges from the eastern coastline of North America is known as the GS Separation Point. **b** Proposed change in the ocean currents during the LIA compared to modern day. The size of the arrows relative to

those in **(a)** denote the change in strength. Note that the locations are purely illustrative of the direction of movement and thus are likely exaggerated and idealised. The black box highlights the location of Bermuda. The abbreviations are as follows: DWBC Deep Western Boundary Current, GS Gulf Stream, LC Labrador Current, NRG Northern Recirculation Gyre, SWC Slope Water Current.

concentrations in stalagmites can exhibit a seasonal signal (e.g., refs. 13,14) that can be employed both as a chronological tool via its seasonal cyclicity and as a climate proxy through its relative values. Stalagmite Mg concentrations can record temperature based on the temperature dependency of Mg's partition coefficient (D_{Mg}) in calcite (e.g., refs. 13,15). However, sea spray contributions to rainfall may also affect dripwater chemistry, especially in island karst systems and, consequently, stalagmite Mg concentrations^{16–19}.

Bermuda's position within the recirculation gyres south of the GS makes it an ideal site to capture the effects of a southward GS shift, and the presence of extensive cave systems offers a rich speleothem archive for climate reconstruction. However, while other SST reconstructions for Bermuda exist (e.g., refs. 20–23), few provide a continuous record spanning more than the last three centuries. Understanding the palaeoclimatic changes experienced in Bermuda on this temporal scale will provide new insights into how the LIA, with its clearly expressed NH climate anomaly, affected GS position and strength^{9,24–26}.

Here, we use the Mg concentrations of a Bermudan stalagmite, which are connected to sea spray contributions to dripwater, to construct a monthly palaeotemperature record spanning 564 years (1449–2013 CE). We derived a Mg-SST calibration based on a regression between our record and a previously developed coral Sr/Ca-SST record²¹. The resulting reconstruction yields SSTs covering most of the LIA and reveals past GS migration patterns at very high temporal resolution and chronological accuracy.

Site description

Leamington Cave in northeastern Bermuda (32° 20' 31.64" N, 64° 42' 30.93" W; entrance at 18 m a.s.l.) is a privately-owned former show cave connected to the ocean via flooded conduits and a large cave pool (Supplementary Fig. 1a). The cave contains many actively growing speleothems above the high tide line, with cave monitoring data revealing a same-day drip rate response to rainfall that suggests residence times capable of preserving a seasonal signal (Supplementary Fig. 2). The Bermuda Islands consist of a carbonate platform above a volcanic seamount and are comprised almost entirely of aeolianites and palaeosols²⁷. The Walsingham Formation, an aeolianite limestone unit (the oldest limestone unit, deposited

approximately 1.1–0.8 Ma), hosts most of Bermuda's caves (including Leamington Cave) and crops out along the eastern border of the Harrington Sound and the western edge of Castle Harbour^{28,29}.

Bermuda has a humid subtropical climate (Cfa in Köppen–Geiger classification³⁰) and lies within the North Atlantic hurricane belt, with the hurricane season running from June to November each year. Meteorological data³¹ indicate that mean SSTs are lowest in February (17.8 °C) and peak in August (28.5 °C) (Supplementary Fig. 1c). May historically experiences the lowest mean monthly rainfall (86.7 mm), whereas October has the highest (161.6 mm)³¹. The hurricane season accounts for a mean of 55% of annual rainfall. Except for September and October, when winds prevail from the east, winds typically come from SW and SSW, reaching a maximum in January (6.01 m/s) and a minimum in September (4.49 m/s)³¹.

Results and discussion

Bermuda temperature trends

Our SST reconstruction for Bermuda is derived from stalagmite BER-SWI-13 using an age model constructed from a Mg cycle count. The cycle count is modelled to a radiocarbon chronology in intervals where cyclicity is less pronounced and is better constrained and more precise than both the radiocarbon and U-Th chronologies (Fig. 2; full details of our chronology and age model construction are discussed in Materials and Methods). By virtue of the inverse relationship between wind speed and SST, our monthly-resolved Mg record serves as an indirect proxy for SST via sea spray contributions to dripwater (Fig. 3). SST estimates were obtained through calibrating the stalagmite Mg record to a previously published coralline SST record ($r = -0.56$, $p \ll 0.001$; 1782–1998²¹); (Fig. 4a, b). The record presented here cannot be confidently compared to observational SST data (starting in 1950) due to anthropogenic influences on speleothem deposition post-1961, likely as a result of land use change above the site (Supplementary Fig. 5). However, because the coral-derived record calibration is derived from a regression with instrumental data²¹, the significant correlation with the stalagmite reconstruction likely reinforces the accuracy of our record, despite the errors being amplified by the additional proxy regression. The resultant record spans 564 years (1449 to 2013 CE), making it one of the longest continuous high-resolution records for the region.

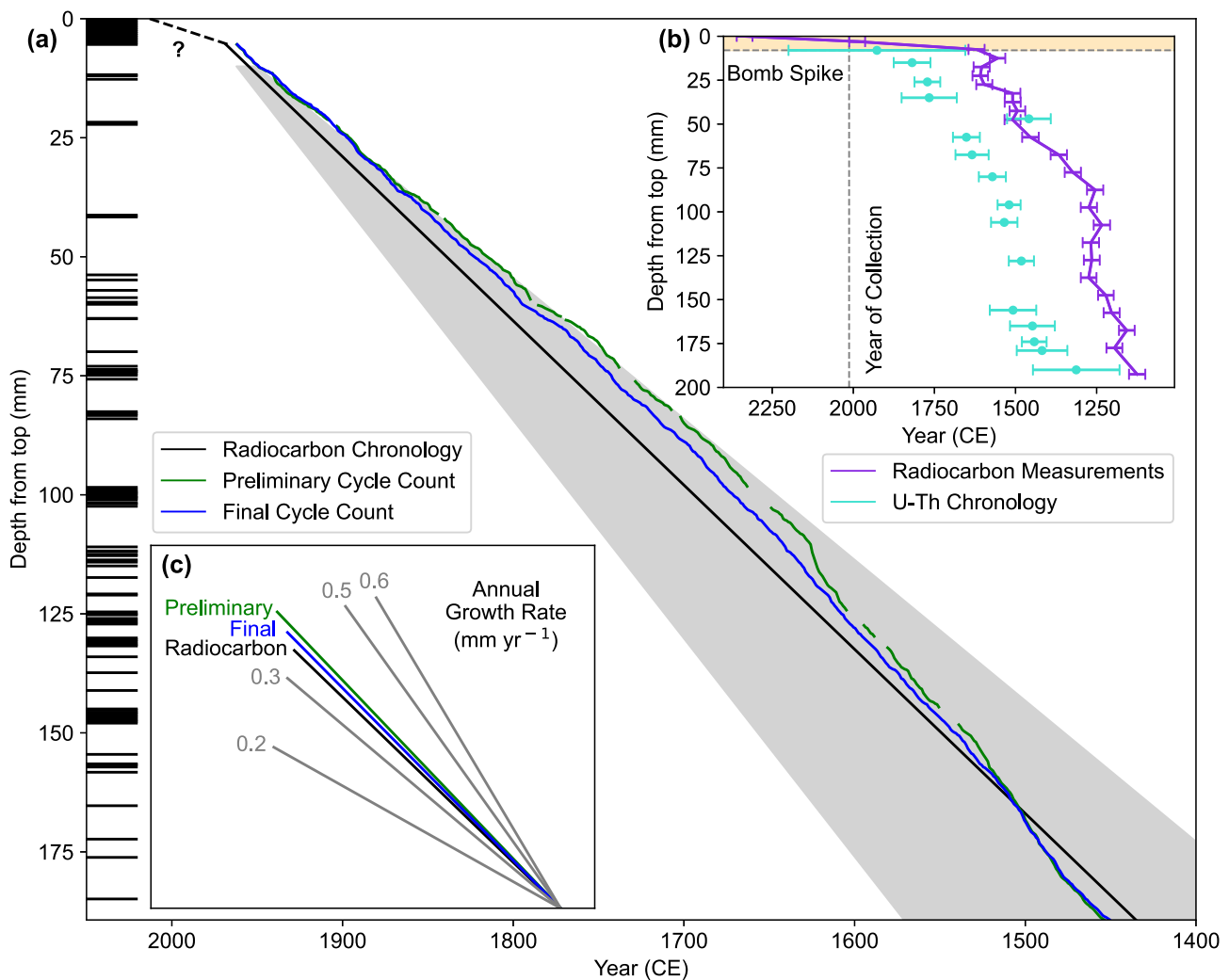


Fig. 2 | Stalagmite BER-SWI-13 chronology. **a** Development of the BER-SWI-13 chronology, comparing the preliminary cycle count (green) and the radiocarbon (black) to the final cycle count (blue), which is developed from both. The grey shaded area signifies the 2σ confidence interval of the radiocarbon chronology. The cycle counts plot outside the radiocarbon chronology errors at the top as the radiocarbon model used a rough estimate for the bomb spike, which was updated in the cycle counts. Black areas (left-hand side) mark depths modelled to the

radiocarbon mean. **b** Radiocarbon data recorded in the stalagmite (purple) compared to the U-Th dates (cyan). The black arrow indicates the trajectory of the radiocarbon data if only influenced by the Suess Effect. Note that the radiocarbon ages here have not been corrected for dead carbon fraction and that the U-Th dates use $(^{238}\text{U}/^{232}\text{Th})_{\text{initial}} = 5 \pm 2.5$. **c** Mean growth rates based on radiocarbon (black, 0.345 mm yr^{-1}), preliminary (green, 0.373 mm yr^{-1}), and final (blue, 0.360 mm yr^{-1}) chronologies.

The stalagmite-derived SST reconstruction exhibits notable agreement with both six previous coralline palaeotemperature records from offshore Bermuda and reanalysis data (Fig. 5 and Supplementary Fig. 10), illustrating its reconstructive power^{20–23,32}. The new stalagmite SST record (Fig. 4) suggests that prior to the 18th century, SSTs were relatively stable, fluctuating within a range of 1.9°C around a mean of 24.6°C (compared to the 1950–2018 average of 22.7°C ³⁰). A cooling trend lasting ~ 130 years began in ~ 1720 CE at a rate of approximately -0.27°C per decade and ended with the onset of the post-1850 warming. The cooling period exhibits high frequency interannual oscillations with decadal-scale fluctuations of $\sim 1.5^\circ\text{C}$ (a range of 4.6°C around a mean of 22.8°C), compared to fluctuations of less than 0.5°C over the same timescale before ~ 1720 CE. A warming trend of $\sim 0.16^\circ\text{C}$ per decade then starts around 1850 CE and lasts the rest of the record. The interannual variance also decreases after 1961 CE, but this is likely the product of anthropogenic impacts on the site's hydrology (e.g., the construction of buildings and land use change above the site) and/or a shallower mixed layer depth^{33,34} rather than changes in climate as the annual signal across that interval is also less pronounced, despite no change in the annual climate signal.

SST proxy records from four independent archives show stable, likely elevated, SSTs from the mid-1400s to the early 1700s (Fig. 5). However, a

coral extension record from the region suggests that SSTs were slightly lower than the stalagmite record indicates and that a brief warming period ensued during the late 1600s (Fig. 5a and c)²³. This could be an example of wind speed artificially amplifying the SST signal in the stalagmite as the period coincides with an extended negative NAO interval (Fig. 5g). Similarly, however, the stalagmite record is in better agreement than the coral extension record with the other available records, and thus other forcing and/or chronological uncertainty could explain the inconsistency. Bermudan coral extension rates have been tied to nutritional pulses associated with negative NAO winters³⁵ and hence temperature is likely not the only control on the proxy³⁶. Additionally, the record's chronology is developed from a layer count which is not supported by other methods and thus could be susceptible to undercounting resulting from low growth rates/hiatuses²¹. Despite this discrepancy, both records agree that SSTs were uncharacteristically high during the LIA. The records then show a cooling trend lasting until the mid-1800s. The coral extension record suggests this cooling lasted until the early 1900s²³. However, two $\delta^{18}\text{O}$ records from different corals (Fig. 5d)²⁰ support the mid-1800s trend reversal seen in the stalagmite and ref. 21 records. All records then show a strong warming trend lasting until the present. Both the reconstruction presented here and the ref. 21 coralline

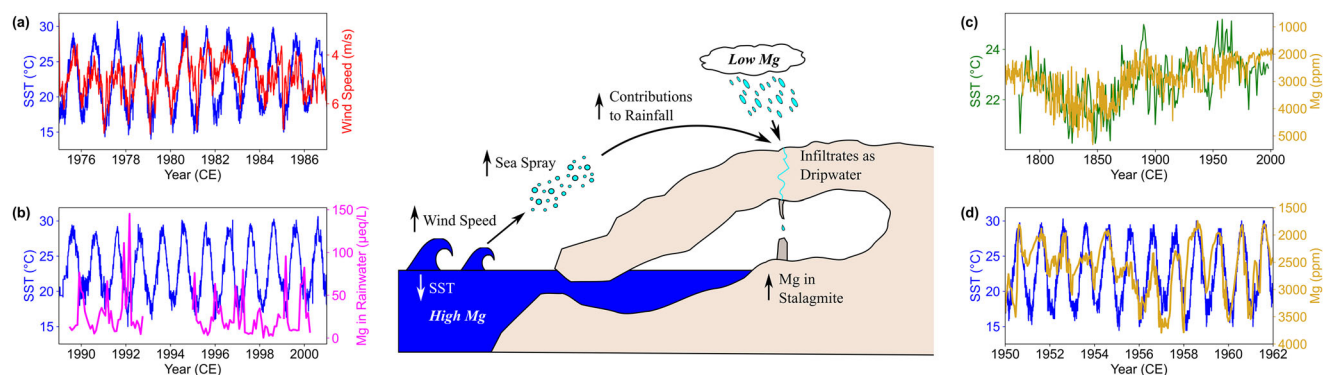


Fig. 3 | Schematic of the proposed Mg-SST proxy mechanisms. **a** Observational wind speed data (red) plotted against observational SST data (blue)³¹. **b** Mg in collected rainwater (magenta)⁸⁹ plotted against the observational SST data in **(a)**. **c** BER-SWI-13 Mg concentrations (gold) shown against Bermudan SSTs reconstructed from a coral (green)²¹. **d** BER-SWI-13 Mg concentrations (gold) shown against the observational SST data in **(a)**. Stalagmite Mg cyclicity is not directly

compared to wind speed or rainwater Mg variability due to potential anthropogenic impacts on the Mg record post-1961 and wind speed and rainwater observations beginning in 1975 and 1989, respectively. Note that the stalagmite Mg and wind speed axes are inverted and that the bold italics in the schematic denote source concentrations (i.e., ocean water is Mg-rich and rainwater has comparatively low Mg concentrations).

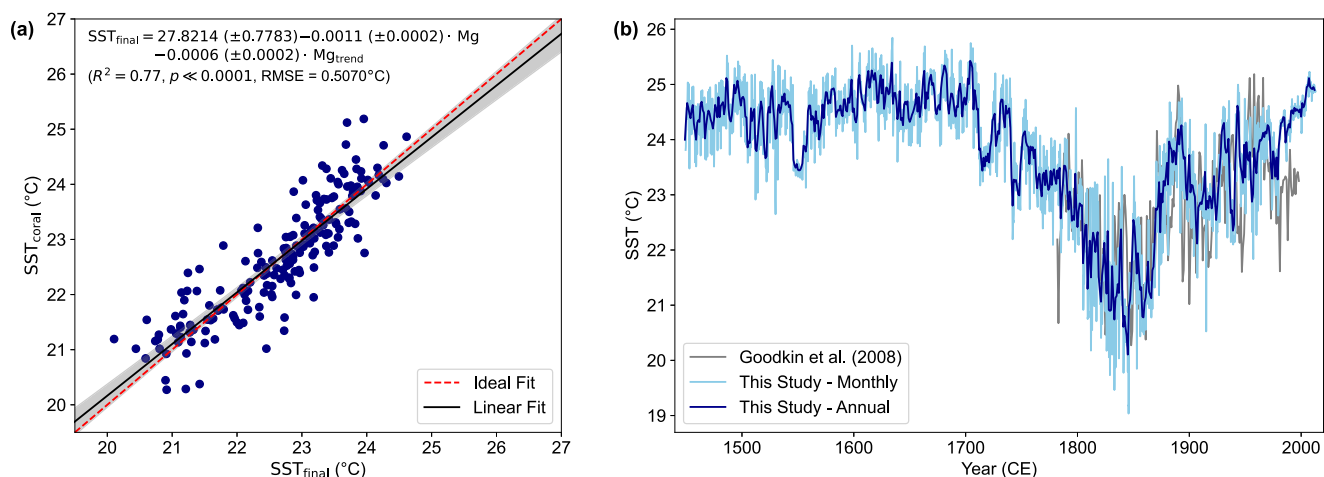


Fig. 4 | The stalagmite-derived SST reconstruction. **a** The model predictions against the warped coralline SSTs. The linear best-fit for these data with 95% confidence interval (grey shading) is compared to that of an ideal relationship (i.e.,

$SST_{final} = SST_{coral}$). **b** The regression model output (1449–2013 CE; 564 years) at both a monthly (light blue) and annual (dark blue) resolution plotted with a coralline SST record (grey; 1782–1998 CE; 217 years) from Bermuda²¹.

record show a brief cooling interval starting in the late 19th century, which lasted around two decades before warming resumed (Fig. 5a, b). The relatively cooler mean SSTs of the 19th and 20th century, when compared to those pre-1720 CE are likely explained by wind speed changes artificially increasing estimates and/or aerosol forcing in the NH reducing SSTs^{37,38}.

Influences on reconstructed SST variability

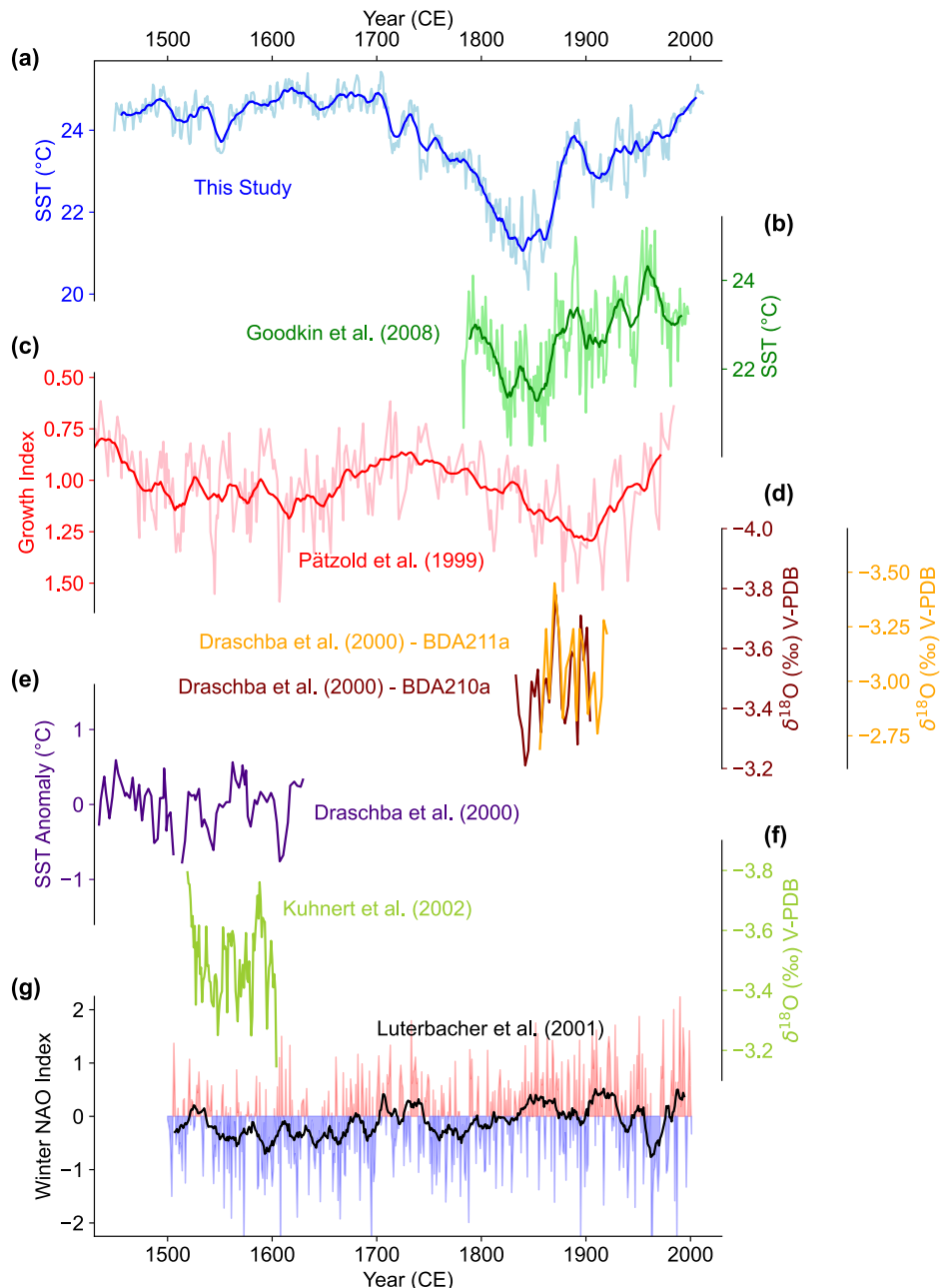
The SST record reconstructed here exhibits three distinct intervals: (1) pre-1700 elevated, stable SSTs; (2) 1700–1850 cooling; and (3) post-1850 warming. Enhanced radiative forcing from additional greenhouse gases and rising total solar irradiance at the end of the LIA are likely to be the cause of the increased temperatures observed after 1850 CE (Fig. 6c and Supplementary Fig. 11). A comparison with NH temperature anomalies, which remained largely low before the mid-1800s (Fig. 6g), highlights that Bermudan SSTs were uncharacteristically high during the LIA, suggesting conditions influenced primarily by natural factors with minimal anthropogenic impact.

Higher latitude palaeotemperature reconstructions exhibit the opposite trends to those seen in Bermuda. *Neogloboquadrina pachyderma* abundances in a sediment core from the northwest Atlantic³⁹ suggest a warming trend beginning in the 18th century (Fig. 6a). Similarly, a temperature record from Chesapeake Bay using the Mg/Ca ratios of ostracodes⁴⁰

exhibits cooler SSTs during the LIA followed by an increase starting in the mid-1700s (Fig. 6b). However, our reconstruction from Bermuda (Fig. 6c) suggests regional ocean temperatures were high during the oldest part of the record (1449–1720 CE) until a cooling trend ensued around 1720 CE, lasting approximately 130 years. The opposing temperature trends in the *N. pachyderma* and Mg/Ca records, compared to the Bermuda reconstruction, suggest an antiphase thermal gradient between the records, whereby an increase in SSTs at lower latitudes leads to a decrease at higher latitudes.

Due to the extended cold intervals, the LIA is associated with expanded sea ice extent, which would have disrupted North Atlantic ocean currents by changing temperature and salinity profiles²⁶. Two mean sortable silt (SS) records from sediment cores off Cape Hatteras (Fig. 6d) suggest that the DWBC was stronger during the LIA before weakened due to enhanced freshwater fluxes³⁹. Similarly, a SS record from a core off the southeastern Grand Banks (Fig. 6d) indicates that the LC was strongest during the LIA (over the last 1.45 ka), likely due to elevated freshwater transport from the Arctic¹⁰. A stronger DWBC and LC would have increased cold water flow southward into the western North Atlantic Ocean, having consequences for wider ocean circulation patterns. Sediment cores near the Dry Tortugas and Great Bahama Bank (Fig. 6e) are thought to have captured Florida Current transport over the last millennium⁹. The reconstruction suggests that the GS was systematically weaker during the LIA by approximately 10%. Modelling

Fig. 5 | Stalagmite-based SST reconstruction compared with various other proxy reconstructions of Bermudan SSTs. a–f Comparison of the stalagmite Mg concentration-based record to six coralline palaeo-ocean temperature records for Bermuda^{20–23} and (g) a normalised winter North Atlantic Oscillation index dataset with 15-point moving average⁴⁴. Note that the ref. 22 record was averaged to annual spacing from monthly to reduce noise and that axes have been inverted to match the direction of the SST axis.



studies (e.g., refs. 41,42) show that both stronger cold, high latitude currents and weaker GS flow cause the GS to move south and reduce northward heat transport¹¹. As Bermudan SSTs are controlled by GS dynamics, a southerly GS path could increase local SSTs and lead to reduced SSTs at higher latitudes. Therefore, the antiphase relationship could be explained by GS path migration during the LIA as a result of changing ocean circulatory patterns. Warming in several cores south of Newfoundland are thought to reflect northward slope water current migration during the LIA⁴³, but our SST record indicates a broader antiphase system suggesting the northward ocean current shift was more widespread.

The high SSTs in our reconstruction are coeval with the persistent negative NAO index during the LIA observed in many NAO reconstructions^{44–48}. For comparison the ref. 44 winter NAO reconstruction (Fig. 6f) is shown, selected for its wide spatial coverage using numerous sites, high temporal resolution, and extensive use in the literature. The NAO index is defined by the normalised pressure difference between the Icelandic Low and the Azores High and modulates mid-latitude westerly strength as well as heat, freshwater, and momentum fluxes in the North Atlantic (e.g.,

ref. 49). Because a negative NAO index is associated with decreased westerly wind strength, the high reconstructed SSTs pre-1700 in Bermuda may be attributable to the proxy's wind speed connection capturing changes in atmospheric phenomena. A weakening of the westerlies at this time could have reduced sea spray over the site and thus led to less Mg incorporation into the stalagmite. These weaker winds are evident in the relatively low implied seawater contribution from the Mg and Sr concentrations at the time (~4.47% compared to the mean ~5.81%; Supplementary Fig. 7). However, considering that a transition in the 18th century can also be seen in sediment core-derived temperature and flow speed reconstructions^{39,40}, there is likely a direct temperature effect in addition to any changes in wind speed. Studies have also found a link between the GS and the NAO^{50,51}. During a more negative NAO phase, decreased heat loss, higher precipitation, and weaker winds reduce convection in the Labrador Sea, corresponding to a weaker AMOC and in turn a more southerly GS path^{49,52}. This is evident in current GS path migration (1993–2016), which may reflect an increasingly negative NAO (e.g., refs. 51,53). Thus, the GS likely did migrate at this time, but the potential for reduced wind speed over Bermuda

to exaggerate the reconstructed SST signal complicates the quantification of the exact southward positional extent of the GS movement. Furthermore, higher frequency variability may also be influenced by other atmospheric phenomena, but the significant agreement with oceanographic data suggests that either oceanic forcing is the salient factor or that oceanic and atmospheric forcing are heavily coupled.

Speleothem Mg concentrations are sensitive to the effects of prior calcite precipitation (PCP) and are often used as a proxy for rainfall amount (e.g., refs. 54,55). However, areas with evenly distributed rainfall throughout the year usually do not exhibit a strong PCP effect^{54,56}. Therefore, a change in cave processes (such as the degree of water-rock interactions or PCP) is unlikely to be the primary driver of Mg concentration variability as they are controlled by broader climatic factors, and only the period after 1961 exhibits the effects of PCP following anthropogenic impacts on the cave system (Supplementary Fig. 7). For this reason, although cave processes or the amount of fluid inclusions may reduce the accuracy of the temperature estimates, the trends exhibited here are likely not exclusive to the BER-SWI-13 record and reflect broader regional trends.

Assuming our SST estimates reflect solely temperature change without amplification due to wind speed, the 2–3 °C temperature change over 130 years suggests a moderately fast rate of GS migration when considering the relatively shallow nearby SST gradient in the modern North Atlantic (Fig. 6), implying that GS position is reasonably sensitive to forcing. Observational data tracking the current northward GS migration detected a shift in the GS north wall of ~1.5° in 52 years (1965–2017) between 50°W and 40°W⁶. Therefore, with the continuation of current trends in the GS and AMOC, the sensitivity of regional temperatures to GS path drift could have serious ramifications for future regional climates, ecosystems, and extreme weather events. Furthermore, the mid-1700s transition seen here agrees with similar trends seen in previous AMOC proxy records (e.g., ref. 39, Supplementary Fig. 11), potentially supporting an earlier onset of AMOC weakening.

Our study reconstructed regional SST using a stalagmite from Bermuda via sea spray contributions to dripwater. A Mg cycle count, modelled to a radiocarbon chronology, yielded a high-precision age model and a monthly-resolved Mg record spanning over five centuries (1449–2013 CE). Owing to the Mg record's significant agreement with SST records but with the opposite directionality to what is expected from Mg's partition coefficient into calcite, the record likely captures SST variability via a connection to wind speed. Palaeo-oceanographic temperature estimates were derived from modelling the Mg concentration record to a previously published coralline proxy SST record²¹. The resultant record indicates temperatures before the early 1700s were consistently high, contrary to more Northerly regional reconstructions and the NH average^{39,40,57}. We propose this anti-phase thermal gradient suggests that the GS migrated northwards towards the end of the LIA following a prior period characterised by a more southerly GS path. Flow speed reconstructions for the GS, DWBC and LC support this interpretation^{9,10,39}, providing evidence of weakening southward currents in the 18th century from strong conditions during the LIA. Further research should focus on quantifying the rates of positional change seen here, to gain a better understanding of GS sensitivity to additional forcing as well as its subsequent manifestations and effects. These results provide evidence of a moderately fast natural GS migration during the LIA. Previous research has proposed changes in ocean circulation towards the end of the LIA (e.g., ref. 39), and our high-resolution SST reconstruction from Bermuda reinforces this concept.

Methods

Stalagmite BER-SWI-13

BER-SWI-13 is a 192 mm long stalagmite that grew in Leamington Cave, Bermuda (Supplementary Fig. 1a, b). The stalagmite was selected for its favourable internal structure and active drip hydrology, which is responsive to rain events⁵⁸ and plots as a near-ideal seasonal flow⁵⁹. Because cave monitoring data revealed a same-day drip rate response to rainfall

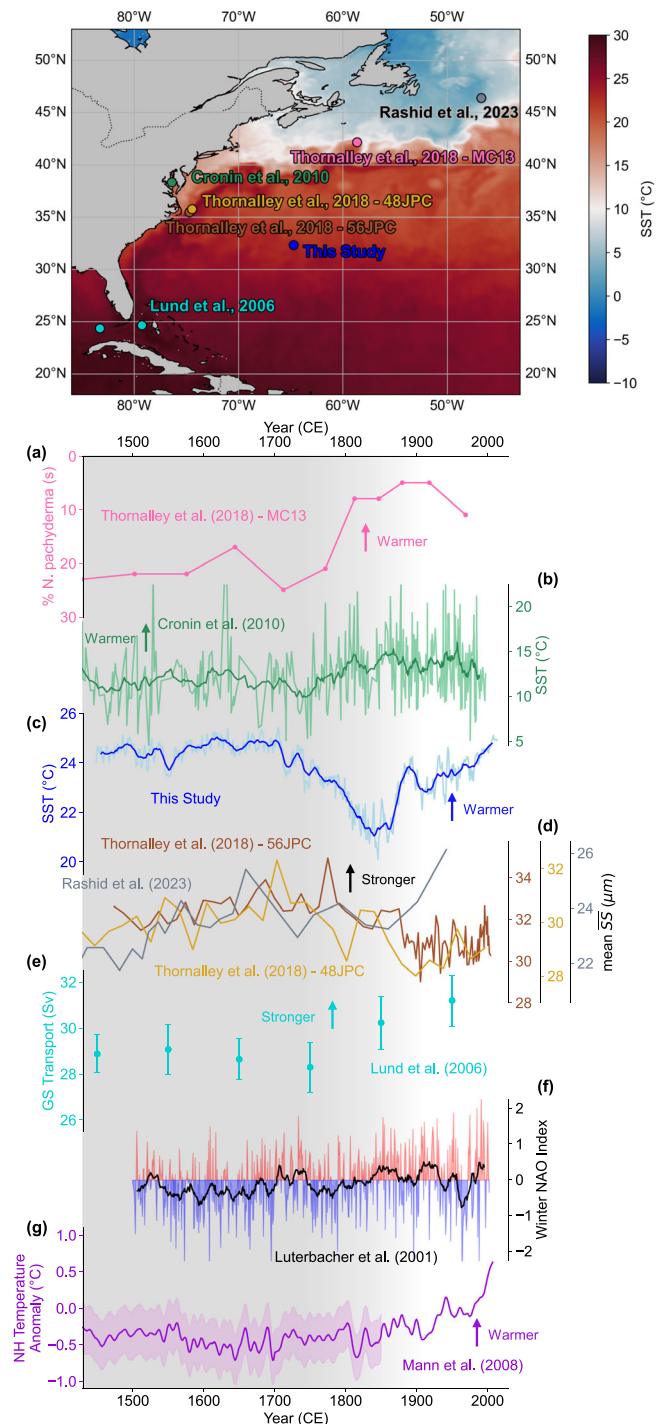


Fig. 6 | Proxy reconstructions of North Atlantic variability. (top) Map of modern observational North Atlantic regional SSTs (2023 mean; $0.1^\circ \times 0.1^\circ$ spatial resolution)⁹⁰. Coloured circles on the map denote the sites of the records in the panel below. (bottom) Palaeoclimatic records for the study period. **a** Percentage abundance of the polar species *N. pachyderma* (sinistral) in a marine sediment core (OCE326-MC13) from the Northwest Atlantic³⁹. **b** Chesapeake Bay reconstructed SST data with a 15-point moving average⁴⁰. **c** The annual SST model for Bermuda with a 15-point moving average. **d** Mean sortable silt (SS) grain size data from three cores (red, 56JPC; orange, 48JPC; grey, MO217)^{10,39}. **e** Gulf Stream transport estimates in the Florida Straits⁹. **f** Normalised winter North Atlantic Oscillation index data with 15-point moving average⁴⁴. **g** Northern Hemisphere temperature anomaly reconstruction with 95% confidence interval for proxy-derived estimates⁵⁷. The grey shaded area denotes the temporal extent of the LIA.

events (Supplementary Fig. 2)⁵⁸, the residence time of the seawater signal is sufficiently low to accurately preserve hydrology-induced seasonality at a monthly-resolution⁵⁹. The cave pool's connection to the ocean promotes daily cave ventilation by tidal flushing, suggesting the stalagmite never experienced condensation corrosion due to CO₂ buildup⁵⁸. Additionally, monitoring data shows daily cave temperature is positively correlated to daily mean SST ($r = 0.83$, $p < 0.01$) (Supplementary Fig. 3)⁵⁸.

U-series and radiocarbon dating

Reconnaissance CT scanning determined the position of stalagmite BER-SWI-13's central growth axis and informed its sectioning. Cut sections were polished and then cleaned in an ultrasonic bath of deionised water (see ref. 58 for full methods). Visual examination after sectioning showed no signs of growth hiatuses (Supplementary Fig. 1b). Sixteen ~400 mg carbonate powder samples (Supplementary Data 1) were milled along the stalagmite growth axis. These were dated using multi-collector inductively coupled plasma mass spectrometric (MC-ICPMS) U-Th methods at the facilities of Bristol Isotope Group, University of Bristol, and University of St. Andrews Isotope Geochemistry (STAiG). U and Th separation and measurement protocols described in ref. 60 were followed, where CRM U112a and an inhouse Th standard (Teddi) was used for bracketing the samples and correcting for instrumental drift in mass bias, SEM yield. We adopt relevant decay constants from ref. 61. U-series data was analysed using the IsoplotR software⁶².

U-Th ages for material that is both young (i.e., <1 ka) and has low $^{238}\text{U}/^{232}\text{Th}$ ratios are poorly constrained because there is no prior knowledge of the $^{230}\text{Th}/^{232}\text{Th}$ ratios at the time of calcite precipitation. Because of this, we attempted to assess the initial Th ratio using isochron methods for two of the milled samples (BER-SWI-UTH-13 and -15) by performing replicate analysis (~100 mg sub-samples). However, there was insufficient $^{238}\text{U}/^{232}\text{Th}$ ratio variation in the two sets of replicate analysis to determine useful estimates of the initial $^{230}\text{Th}/^{232}\text{Th}$ component.

Most researchers use an estimate of initial Th assuming it is equivalent to bulk Earth silicate composition ($^{238}\text{U}/^{232}\text{Th} = 0.8 \pm 0.4$) as a starting point. However, there are many examples of elevated values of this ratio where either carbonate dust with high U/Th or hydrogenous elements in cave drip waters have probably influenced the isotopic composition: see review by Richards and Dorale⁶³ and recent papers by refs. 64,65. Other speleothem samples from the North Atlantic and Caribbean region, including the Bahamas, Yucatan, and Puerto Rico, have been similarly affected^{66–71}.

In the absence of sufficiently robust estimates of the initial Th ratio via isochron methods, we considered the principle of stratigraphic constraint (see ref. 72) and adopted an elevated value ($(^{238}\text{U}/^{232}\text{Th})_{\text{initial}} = 5 \pm 2.5$) that eliminates the major age inversion at the top of the sample (Supplementary Fig. 4) that is evident when using the bulk Earth initial Th ratios. Using this elevated value also shifts the basal age (BER-SWI-UTH-16) younger and would suggest a growth rate for the oldest material that is closer to that exhibited for the rest of the speleothem. One anomalous age remains for the sample (BER-SWI-UTH-5), which is likely to have been affected by post-depositional alteration.

Additionally, twenty-five 8–9 mg carbonate powder samples were milled for ^{14}C analysis (Supplementary Data 2) using a semi-automatic high-precision drill (Sherline 5400 Deluxe) at ETH Zurich. The ^{14}C samples were milled in increments of 5 mm for the top 50 mm, and 10 mm for the remaining 140 mm⁵⁸. The top ~0.1 mm was discarded for each ^{14}C sample. Potential contamination during sub-sampling was minimised by cleaning all tools with methanol and drying with compressed air in between samples. Carbonate samples were prepared for accelerator mass spectrometry analysis by graphitisation at the Laboratory for Ion Beam Physics of ETH Zurich. The samples were processed on an automatic graphitisation system coupled to a carbonate-handling system (CHS-AGE, Ionplus, Switzerland) by acidification to CO₂ using 2 mL of 85% H₃PO₄ and followed by graphitisation using excess H₂ over Fe catalyst. Radiocarbon contents were measured on a MICADAS accelerator mass spectrometer (Ionplus) following standard protocols for quality and blank assessment: oxalic acid II

(NIST SRM 4990 C) was used as the normalising standard, measured to a precision of better than 2‰. We used IAEA-C1 as a blank and IAEA-C2 and a modern coral standard as secondary standards. The procedural blank was established using a ^{14}C -free stalagmite (MAW-1, ~170 kyr old).

Trace element analysis

Trace element concentrations were measured using the prototype RESOLUTION M-50 excimer (193 nm) laser-ablation system with a two-volume laser-ablation cell coupled to an Agilent 7500ce/cs quadrupole ICPMS at Royal Holloway University, London^{73–75}.

Ablation tracks were pre-ablated to remove any superficial contamination and measured using a 140 by 10 μm rectangular laser slit across 50 mm sectioned blocks on the opposite half to the carbonate sampling. Sectioning was slightly off perpendicular to the growth direction so that overlaps in transects could compensate for any missing data between sections. A 15 Hz laser repetition rate and a laser fluence of ~4 J/cm² with a stage scan speed of 10 $\mu\text{m s}^{-1}$ of the LA cell were used during the continuous main track measurement⁷³. Speleothem analyses were bracketed by analyses of NIST 612, NIST 610 for quantification using ^{43}Ca as internal standard⁷⁶, and MACS3 standards for accuracy control (see ref. 77).

The resultant data were then reduced using the Iolite software package, using NIST 610/612 standards for external standardisation⁷⁸. Trace element analyses using similar techniques have achieved accuracies better than 5%^{74,77}.

BER-SWI-13 chronology

The U-Th chronology suggests an unusual range in speleothem growth rate for a humid subtropical cave environment (65 to 1636 $\mu\text{m yr}^{-1}$; where the 90th percentile of annual layers in a global review¹² is 404 $\mu\text{m yr}^{-1}$). This variability is most pronounced between depths from top of 26 and 35 mm where the growth rate implied from U-Th dating suddenly rises from 233 $\mu\text{m yr}^{-1}$ to 1636 $\mu\text{m yr}^{-1}$ for 5.5 years before returning to 196 $\mu\text{m yr}^{-1}$, despite no hiatuses being observed. Additionally, the carbonate samples returned consistently low U concentrations of 83–136 ng/g, except for two samples that are 299 and 362 ng/g. The low U concentrations and unrealistically high variations in growth rate suggest that a chronology based solely on U-Th dating would yield less accurate results than radiocarbon methods after dead carbon fraction correction. For this reason, we use the U-Th chronology only as confirmation when developing an alternative chronology based on radiocarbon dating and annual Mg cycle counting. First, we developed an 'average' chronological model using the radiocarbon-based technique presented in ref. 79 and refined in ref. 80. The model aligns the stalagmite radiocarbon data with known atmospheric radiocarbon levels at the time of carbonate deposition, thus correcting for DCF effects. DCF is assumed to be stationary (i.e., fluctuating around a constant mean value) and trends are detected using hydrology connected proxies (Mg/Ca and $\delta^{13}\text{C}$), but small variations around a long-term mean are allowed thus permitting the use of this technique on the BER-SWI-13 record. The chronology produced this way is anchored to a point of known age, which in our case is given by the clear increase in ^{14}C indicating the rise of the atmospheric bomb spike at 1955 CE (Fig. 2b). The bomb spike was identified using the anomalous rise in raw ^{14}C ages at a depth of approximately 8 mm, which can only be related to the rise in atmospheric ^{14}C through nuclear bomb testing in the 1950–1960s, as it results in much too young ^{14}C ages to be reflecting natural variability. To precisely constrain the depth of the bomb spike inflection point (i.e., the point where the bomb spike begins, our chronological marker), we extrapolated the trends of the data points immediately before (4) and after (3) the visible bomb spike rise. The stalagmite collection year (2013 CE) provides a second chronological anchor. However, owing to possible localised anthropogenic influences on the stalagmite's drip hydrology (e.g., land use change above the cave related to the development of the cave for tourism) starting ~1961 CE, we do not consider data post-1961 in our interpretations (Supplementary Fig. 5).

First the radiocarbon age model defines an initial long-term average growth rate by computing a best fit through all the stalagmite ^{14}C activity

measurements, with an assumed constant atmospheric ^{14}C . This enables each sample to be assigned an approximate age. The model then iterates through adjusting the growth rate in line with atmospheric ^{14}C values from an IntCal13 calibration curve⁸¹ and updating the assigned ages accordingly until the growth rate term converges. Thus, one of the underlying assumptions of the model is that the stalagmite growth rate remains relatively constant and thus the output chronology is a near perfect straight line. However, the error in this assumption is propagated with the depth uncertainty incurred by sampling. Therefore, most of the uncertainty lies with the growth rate estimate and hence leads to very conservative errors that increase with distance from the anchor point and follow near straight lines. This technique is similar to methods used in other geochronological fields, such as ^{210}Pb dating⁸² or ^{230}Th excess dating⁸³ of sediments and has been used to accurately date stalagmites in previous studies (e.g., refs. 84,85).

The LA-ICPMS-derived Mg profiles exhibit well-developed cyclicity through much of the record. A comparison between the number of Mg cycles in the record and the U-Th and radiocarbon chronologies strongly suggests that the Mg cycles are annual. We conducted multiple Mg cycle counts with different observers to test their reproducibility, and constructed a chronology based on the annual Mg cycles (Fig. 2). The post-1961 loss of cyclicity prevents counting cycles relative to the collection year and instead cycles were counted relative to the bomb spike depth, which was adjusted to match a local minimum to obtain a sub-annually resolved chronological anchor. This cyclicity is ambiguous for some sections of the record; thus, in the final cycle count these sections were modelled using the radiocarbon chronology mean growth rate (Supplementary Fig. 6).

Mg concentrations in BER-SWI-13 are significantly inversely correlated ($r = -0.56$, $p \ll 0.0001$, $n = 217$) with a previously developed coral Sr/Ca-derived proxy SST record from Bermuda²¹, which is contrary to that is expected based on the temperature dependency of D_{Mg} . Instead, Mg concentrations appear to be an indirect proxy for SST via sea spray contributions to rainfall (Fig. 3). A clear inverse relationship exists between SST and wind speed (Fig. 3). Colder temperatures are associated with higher wind speeds, which gives rise to higher sea spray contributions to rainfall and vadose dripwater. Seawater has a much higher Mg concentration than normal meteoric water and this influences the concentrations in cave dripwaters (and secondary calcite precipitates such as stalagmites). Additionally, because the Mg and Sr data do not plot along a PCP vector (Supplementary Fig. 7), PCP is unlikely to be a dominant control on the record. The post-1961 CE data appear to show evidence of PCP supporting our decision to exclude these data from our interpretations due to alterations to the stalagmite's drip hydrology. However, the Mg and Sr data do plot along a mixing curve between the concentrations of the bedrock and marine aerosols (Supplementary Fig. 7), supporting the perspective that sea spray (in turn controlled by SST) was the dominant control on Mg and Sr concentrations.

By virtue of the inverse relationship between speleothem Mg and SST, the Mg cycle count was tuned intra-annually so that the Mg concentration minima were assigned a decimal date corresponding to the 15th of August (midway between the months with the lowest mean wind speed) and maxima (determined by the broad shape of the cycle to avoid individual weather events) were assigned a date corresponding to January 1st (start of month with the highest mean wind speed). The resultant high-precision final cycle count (1449–2013 CE) is consistent with the radiocarbon chronology, with a nearly identical mean growth rate (Fig. 2a), as well as high intra-annual precision. The final cycle count yields markedly younger values than the U-Th data until depths from top greater than ~140 mm, when the U-Th growth rate rapidly increases, whilst also having a more consistent annual growth rate (range in annual cycle length—final cycle count: $865.8 \mu\text{m yr}^{-1}$; U-Th: $1571.8 \mu\text{m yr}^{-1}$). The CONstructing Proxy Records from Age models (COPRA) algorithm⁸⁶ was used to develop an age-depth model with cycle count annual maxima and minima as inputs. The resultant COPRA model incorporated 2000 Monte Carlo simulations and piecewise cubic Hermite interpolating polynomial interpolation to assign precise ages to every data point. The COPRA algorithm did not

identify any hiatuses in the record. The complete dataset consists of 18,471 data points and creates a record of sub-monthly resolution with an average of 32.8 values per year.

Mg-SST calibration

To derive SST estimates, the speleothem Mg record was interpolated to monthly spacing and passed through a five-point Savitzky–Golay filter to remove the influence of weather extrema and/or areas with anomalously high amounts of fluid inclusion before averaging into annual values. The correlation between the annual stalagmite Mg concentration record and the annual coralline SST record²¹ over the ~200 years of overlap was then optimised by shifting the SST record within dating uncertainties using dynamic time warping (DTW) with a maximum shift term equal to 25 years to avoid overfitting (see Supplementary Fig. 8). The DTW applied offset was negative (mean of –13.8 years) before 1866 CE, after which it changes to positive (mean of 0.6 years), likely due to the change in trend in both records around this time. It is thought that undercounting is most prevalent in their record before the mid-1800s when growth rates were extremely slow²¹, supporting the negative DTW offset before 1866. Given the difference in magnitude between the Mg (range: 1759–4769 ppm; mean: 3074 ppm; standard deviation: 632 ppm) and SST (range: 20.3–25.2 °C; mean: 22.7 °C; standard deviation: 1.1 °C) values, both series were standardised prior to regression to ensure numerical stability. An initial ordinary least squares linear regression returned autocorrelated residuals (Durbin–Watson statistic: 0.906). Therefore, both series were detrended for subsequent modelling using a five-point centred moving average, with the window size optimised based on residual autocorrelation. A linear regression of both standardised residual series yields the following equation:

$$\epsilon_{\text{SST}} = -0.0004 (\pm 0.0448) - 0.6360 (\pm 0.1025) \cdot \epsilon_{\text{Mg}} \quad (1)$$

(2 σ , 95% conf., $R^2 = 0.46$, $p \ll 0.0001$, RMSE = 0.3027)

To return accurate SST estimates, the inverse of trend of the predictor series was added to the series obtained from the regression, and the result was then transformed back to non-standardized form using the mean and standard deviation of the target series. Thus, the full equation can be written as:

$$\text{SST}_{\text{final}} = \left((\beta_0 + \beta_1 \cdot \epsilon_{\text{Mg}}) + -\text{Mg}_{\text{trend}} \right) \cdot \sigma_{\text{CoralSST}} + \mu_{\text{CoralSST}} \quad (2)$$

where β_0 and β_1 are the coefficients of the linear regression of the processed data; ϵ_{Mg} is the standardised, residual Mg after detrending; Mg_{trend} is the smoothed standardised Mg series; and σ_{CoralSST} and μ_{CoralSST} are the standard deviation and mean of the warped SST data, respectively. Substituting in the derived coefficients and propagating the errors to derive an equation in non-standardised space yields:

$$\text{SST}_{\text{final}} = 27.8214 (\pm 0.7783) - 0.0011 (\pm 0.0002) \cdot \text{Mg} - 0.0006 (\pm 0.0002) \cdot \text{Mg}_{\text{trend}} \quad (3)$$

(2 σ , 95% conf., $R^2 = 0.77$, $p \ll 0.0001$, RMSE = 0.5070 °C)

The modelled stalagmite SST record (Supplementary Data 3) has less variance than the coralline record (Fig. 4a) despite its near-ideal relationship, likely because of aquifer mixing smoothing the signal (potentially the mixing of diffuse and concentrated flow paths). The signal-dampening effect that the strong correlation between cave temperature and SST would have via the temperature dependency of Mg fractionation may also be responsible for this reduced variance. For this reason, the record's ability to capture variations in seasonal signals is hindered and so we interpret the record at annual resolution. Additionally, the regression's predictive power was evaluated using split-period calibration/verification tests in both directions (see Supplementary Fig. 9). The regression passed these tests and thus yielded both a monthly and an annual SST record spanning over five centuries years, making it longer and higher resolution than many previous SST records from the region (Fig. 4).

Data availability

All the data needed to evaluate the conclusions in the paper are available in the paper and/or the Supplementary Information. The underlying data are also available from <https://doi.org/10.5281/zenodo.15477169> (ref. 87).

Received: 17 February 2025; Accepted: 4 June 2025;
Published online: 14 July 2025

References

- Ditlevsen, P. & Ditlevsen, S. Warning of a forthcoming collapse of the Atlantic meridional overturning circulation. *Nat. Commun.* **14**, 1–12 (2023).
- Boers, N. Observation-based early-warning signals for a collapse of the Atlantic Meridional Overturning Circulation. *Nat. Clim. Change* **11**, 680–688 (2021).
- van Westen, R. M., Kliphuis, M. & Dijkstra, H. A. Physics-based early warning signal shows that AMOC is on tipping course. *Sci. Adv.* **10**, eadk1189 (2024).
- Palter, J. B. The role of the Gulf Stream in European climate. *Annu. Rev. Mar. Sci.* **7**, 113–137 (2015).
- Caesar, L., Rahmstorf, S., Robinson, A., Feulner, G. & Saba, V. Observed fingerprint of a weakening Atlantic Ocean overturning circulation. *Nature* **556**, 191–196 (2018).
- Caesar, L., McCarthy, G. D., Thornalley, D. J. R., Cahill, N. & Rahmstorf, S. Current Atlantic meridional overturning circulation weakest in last millennium. *Nat. Geosci.* **14**, 118–120 (2021).
- Seidov, D., Mishonov, A., Reagan, J. & Parsons, R. Resilience of the Gulf Stream path on decadal and longer timescales. *Sci. Rep.* **9**, 11549 (2019).
- Whitney, N. M. et al. Rapid 20th century warming reverses 900-year cooling in the Gulf of Maine. *Commun. Earth Environ.* **3**, 179 (2022).
- Lund, D. C., Lynch-Stieglitz, J. & Curry, W. B. Gulf Stream density structure and transport during the past millennium. *Nature* **444**, 601–604 (2006).
- Rashid, H., Zhang, Z. W., Piper, D. J. W., Patro, R. & Xu, Y. P. Impact of Medieval Climate Anomaly and Little Ice Age on the Labrador current flow speed and the AMOC reconstructed by the sediment dynamics and biomarker proxies. *Palaeogeogr. Palaeoclimatol. Palaeoecol.* **620**, 111558 (2023).
- Thibodeau, B. et al. Last century warming over the Canadian Atlantic shelves linked to weak Atlantic Meridional Overturning Circulation. *Geophys. Res. Lett.* **45**, 12376–12385 (2018).
- Baker, A. et al. The properties of annually laminated Stalagmites-A Global synthesis. *Rev. Geophys.* **59**, e2020RG000722 (2021).
- Carlson, P. E., Miller, N. R., Banner, J. L., Breecker, D. O. & Casteel, R. C. The potential of near-entrance stalagmites as high-resolution terrestrial paleoclimate proxies: application of isotope and trace-element geochemistry to seasonally-resolved chronology. *Geochim. Cosmochim. Acta* **235**, 55–75 (2018).
- Huang, Y. M. et al. Seasonal variations in Sr, Mg and P in modern speleothems (Grotta di Ernesto, Italy). *Chem. Geol.* **175**, 429–448 (2001).
- Drysdale, R. et al. Magnesium in subaqueous speleothems as a potential palaeotemperature proxy. *Nat. Commun.* **11**, 5027 (2020).
- Baldini, L. M. et al. Regional temperature, atmospheric circulation, and sea-ice variability within the Younger Dryas Event constrained using a speleothem from northern Iberia. *Earth Planet. Sci. Lett.* **419**, 101–110 (2015).
- Fairchild, I. J. et al. Controls on trace element (Sr-Mg) compositions of carbonate cave waters: implications for speleothem climatic records. *Chem. Geol.* **166**, 255–269 (2000).
- Sinclair, D. J. et al. Magnesium and strontium systematics in tropical speleothems from the Western Pacific. *Chem. Geol.* **294**, 1–17 (2012).
- Tremaine, D. M. et al. A two-year automated dripwater chemistry study in a remote cave in the tropical south Pacific: using Cl– as a conservative tracer for seasalt contribution of major cations. *Geochim. Cosmochim. Acta* **184**, 289–310 (2016).
- Draschba, S., Pätzold, J. & Wefer, G. North Atlantic climate variability since AD 1350 recorded in $\delta^{18}\text{O}$ and skeletal density of Bermuda corals. *Int. J. Earth Sci.* **88**, 733–741 (2000).
- Goodkin, N. F., Hughen, K. A., Curry, W. B., Doney, S. C. & Ostermann, D. R. Sea surface temperature and salinity variability at Bermuda during the end of the Little Ice Age. *Paleoceanography* **23**, PA3203 (2008).
- Kuhnert, H., Pätzold, J., Schnetger, B. & Wefer, G. Sea-surface temperature variability in the 16th century at Bermuda inferred from coral records. *Palaeogeogr. Palaeoclimatol. Palaeoecol.* **179**, 159–171 (2002).
- Pätzold, J., Bickert, T., Flemming, B., Grobe, H. & Wefer, G. Holozänes Klima des Nordatlantiks rekonstruiert aus massiven Korallen von Bermuda. *Nat. Mus.* **129**, 165–177 (1999).
- Broecker, W. S. Was a change in thermohaline circulation responsible for the Little Ice Age? *Proc. Natl. Acad. Sci. USA* **97**, 1339–1342 (2000).
- Lapointe, F. & Bradley, R. S. Little Ice Age abruptly triggered by intrusion of Atlantic waters into the Nordic Seas. *Sci. Adv.* **7**, eabi8230 (2021).
- Schleussner, C. F., Divine, D. V., Donges, J. F., Miettinen, A. & Donner, R. V. Indications for a North Atlantic ocean circulation regime shift at the onset of the Little Ice Age. *Clim. Dyn.* **45**, 3623–3633 (2015).
- Vacher, H. L., Hearty, P. & Rowe, M. P. Stratigraphy of Bermuda: Nomenclature, concepts, and status of multiple systems of classification. In *Terrestrial and Shallow Marine Geology of the Bahamas and Bermuda* (eds Curran, H. A. & White, B.), Vol. 300, 271–294 (1995).
- Hearty, P. J. & Vacher, H. L. Quaternary stratigraphy of Bermuda - a High-resolution pre-Sangamonian rock record. *Quat. Sci. Rev.* **13**, 685–697 (1994).
- Iliffe, T. M. & Calderón-Gutiérrez, F. Bermuda's Walsingham caves: a global hotspot for anchialine stygobionts. *Diversity* **13**, 352 (2021).
- Peel, M. C., Finlayson, B. L. & McMahon, T. A. Updated world map of the Koppen-Geiger climate classification. *Hydrol. Earth Syst. Sci.* **11**, 1633–1644 (2007).
- Bermuda Weather Service. *Climate Data* <https://www.weather.bm/climate.asp> (2018).
- Rayner, N. A. et al. Global analyses of sea surface temperature, sea ice, and night marine air temperature since the late nineteenth century. *J. Geophys. Res.-Atmos.* **108**, 4407 (2003).
- Michaels, A. F. & Knap, A. H. Overview of the US JGOFS Bermuda Atlantic time-series study and the hydrostation S program. *Deep Sea Res. Part II: Topical Stud. Oceanogr.* **43**, 157–198 (1996).
- Steinberg, D. K. et al. Overview of the US JGOFS Bermuda Atlantic time-series study (BATS): a decade-scale look at ocean biology and biogeochemistry. *Deep Sea Res. Part II: Topical Stud. Oceanogr.* **48**, 1405–1447 (2001).
- Courtney, T. A., Kindeberg, T. & Andersson, A. J. Coral calcification responses to the North Atlantic Oscillation and coral bleaching in Bermuda. *PLoS One* **15**, e0241854 (2020).
- Tierney, J. E. et al. Tropical sea surface temperatures for the past four centuries reconstructed from coral archives. *Paleoceanography* **30**, 226–252 (2015).
- Booth, B. B. B., Dunstone, N. J., Halloran, P. R., Andrews, T. & Bellouin, N. Aerosols implicated as a prime driver of twentieth-century North Atlantic climate variability. *Nature* **484**, 228–232 (2012).
- Wild, M. Global dimming and brightening: a review. *J. Geophys. Res.: Atmos.* **114**, D00D16 (2009).
- Thornalley, D. J. R. et al. Anomalously weak Labrador Sea convection and Atlantic overturning during the past 150 years. *Nature* **556**, 227–230 (2018).

40. Cronin, T. M. et al. The medieval climate anomaly and Little Ice Age in Chesapeake Bay and the North Atlantic Ocean. *Palaeogeogr. Palaeoclimatol. Palaeoecol.* **297**, 299–310 (2010).
41. Neto, A. G., Palter, J. B., Xu, X. & Fratantoni, P. Temporal variability of the Labrador current pathways around the tail of the Grand Banks at intermediate depths in a high-resolution ocean circulation model. *J. Geophys. Res.: Oceans* **128**, e2022JC018756 (2023).
42. Joyce, T. M., Kwon, Y. O., Seo, H. & Ummenhofer, C. C. Meridional Gulf Stream shifts can influence wintertime variability in the North Atlantic Storm track and Greenland blocking. *Geophys. Res. Lett.* **46**, 1702–1708 (2019).
43. Keigwin, L. D. & Pickart, R. S. Slope water current over the Laurentian Fan on interannual to millennial time scales. *Science* **286**, 520–523 (1999).
44. Luterbacher, J. et al. Extending North Atlantic Oscillation reconstructions back to 1500. *Atmos. Sci. Lett.* **2**, 114–124 (2001).
45. Hernández, A. et al. A 2,000-year Bayesian NAO reconstruction from the Iberian Peninsula. *Sci. Rep.* **10**, 14961 (2020).
46. Baker, A., Hellstrom, J. C., Kelly, B. F. J., Mariethoz, G. & Trouet, V. A composite annual-resolution stalagmite record of North Atlantic climate over the last three millennia. *Sci. Rep.* **5**, 10307 (2015).
47. Wassenburg, J. A. et al. Moroccan speleothem and tree ring records suggest a variable positive state of the North Atlantic Oscillation during the Medieval Warm Period. *Earth Planet. Sci. Lett.* **375**, 291–302 (2013).
48. Esper, J. et al. Long-term drought severity variations in Morocco. *Geophys. Res. Lett.* **34**, L17702 (2007).
49. Zhang, W. Z., Chai, F., Xue, H. J. & Oey, L. Y. Remote sensing linear trends of the Gulf Stream from 1993 to 2016. *Ocean Dyn.* **70**, 701–712 (2020).
50. Sanchez-Franks, A., Hameed, S. & Wilson, R. E. The Icelandic low as a predictor of the Gulf Stream North Wall Position. *J. Phys. Oceanogr.* **46**, 817–826 (2016).
51. Taylor, A. H. & Stephens, J. A. The North Atlantic oscillation and the latitude of the Gulf Stream. *Tellus Ser. a-Dyn. Meteorol. Oceanogr.* **50**, 134–142 (1998).
52. Medhaug, I., Langehaug, H. R., Eldevik, T., Furevik, T. & Bentsen, M. Mechanisms for decadal scale variability in a simulated Atlantic meridional overturning circulation. *Clim. Dyn.* **39**, 77–93 (2012).
53. Chaudhuri, A. H., Gangopadhyay, A. & Bisagni, J. J. Response of the Gulf Stream transport to characteristic high and low phases of the North Atlantic Oscillation. *Ocean Model.* **39**, 220–232 (2011).
54. Jia, W. et al. Highly resolved $\delta^{13}\text{C}$ and trace element ratios of precisely dated stalagmite from northwestern China: hydroclimate reconstruction during the last two millennia. *Quat. Sci. Rev.* **291**, 107473 (2022).
55. Wassenburg, J. A. et al. Calcite Mg and Sr partition coefficients in cave environments: implications for interpreting prior calcite precipitation in speleothems. *Geochim. Cosmochim. Acta* **269**, 581–596 (2020).
56. Denniston, R. F. et al. A Last Glacial Maximum through middle Holocene stalagmite record of coastal Western Australia climate. *Quat. Sci. Rev.* **77**, 101–112 (2013).
57. Mann, M. E. et al. Proxy-based reconstructions of hemispheric and global surface temperature variations over the past two millennia. *Proc. Natl. Acad. Sci. USA* **105**, 13252–13257 (2008).
58. Walczak, I. *Holocene Climate Variability Revealed using Geochemistry and Computed Tomography Scanning of Stalagmites from the North Atlantic Basin*. Doctoral thesis (Durham University, Durham, United Kingdom, 2016).
59. Baldini, J. U. L. et al. Detecting and quantifying palaeoseasonality in stalagmites using geochemical and modelling approaches. *Quat. Sci. Rev.* **254**, 106784 (2021).
60. Hoffmann, D. L. et al. Procedures for accurate U and Th isotope measurements by high precision MC-ICPMS. *Int. J. Mass Spectrom.* **264**, 97–109 (2007).
61. Cheng, H. et al. Improvements in ^{230}Th dating, ^{230}Th and ^{234}U half-life values, and U–Th isotopic measurements by multi-collector inductively coupled plasma mass spectrometry. *Earth Planet. Sci. Lett.* **371**, 82–91 (2013).
62. Vermeesch, P. IsoplotR: A free and open toolbox for geochronology. *Geosci. Front.* **9**, 1479–1493 (2018).
63. Richards, D. A. & Dorale, J. A. Uranium-series chronology and environmental applications of speleothems. *Rev. Mineral. Geochem.* **52**, 407–460 (2003).
64. Wortham, B. E., Banner, J. L., James, E. W., Edwards, R. L. & Loewy, S. Application of cave monitoring to constrain the value and source of detrital $^{230}\text{Th}/^{232}\text{Th}$ in speleothem calcite: implications for U-series geochronology of speleothems. *Palaeogeogr., Palaeoclimatol., Palaeoecol.* **596**, 110978 (2022).
65. Huang, S. et al. An integrated study of constraining the initial ^{230}Th of a stalagmite and its implications. *Quat. Geochronol.* **80**, 101497 (2024).
66. Moseley, G. E. et al. Early–middle Holocene relative sea-level oscillation events recorded in a submerged speleothem from the Yucatán Peninsula, Mexico. *Holocene* **25**, 1511–1521 (2015).
67. Beck, J. W. et al. Extremely large variations of atmospheric ^{14}C concentration during the last glacial period. *Science* **292**, 2453–2458 (2001).
68. Hoffmann, D. L. et al. Towards radiocarbon calibration beyond 28 ka using speleothems from the Bahamas. *Earth Planet. Sci. Lett.* **289**, 1–10 (2010).
69. Fensterer, C. et al. Cuban stalagmite suggests relationship between Caribbean precipitation and the Atlantic Multidecadal Oscillation during the past 1.3 ka. *Holocene* **22**, 1405–1412 (2012).
70. Rivera-Collazo, I. et al. Human adaptation strategies to abrupt climate change in Puerto Rico ca. 3.5 ka. *Holocene* **25**, 627–640 (2015).
71. Warken, S. F. et al. Persistent link between Caribbean precipitation and Atlantic Ocean circulation during the Last Glacial revealed by a speleothem record from Puerto Rico. *Paleoceanogr. Paleoclimatol.* **35**, e2020PA003944 (2020).
72. Hellstrom, J. U–Th dating of speleothems with high initial ^{230}Th using stratigraphical constraint. *Quat. Geochronol.* **1**, 289–295 (2006).
73. Jamieson, R. A. *Trace Element Geochemistry of Belizean and Bermudan Stalagmites: New Tools, Proxies and Applications*. Doctoral thesis (Durham University, Durham, United Kingdom, 2017).
74. Evans, D., Erez, J., Oron, S. & Müller, W. Mg/Ca-temperature and seawater-test chemistry relationships in the shallow-dwelling large benthic foraminifera *Operculina ammonoides*. *Geochim. Cosmochim. Acta* **148**, 325–342 (2015).
75. Müller, W., Shelley, M., Miller, P. & Broude, S. Initial performance metrics of a new custom-designed ArF excimer LA-ICPMS system coupled to a two-volume laser-ablation cell. *J. Anal. At. Spectrom.* **24**, 209–214 (2009).
76. Longerich, H., Jackson, S. & Gunther, D. Laser ablation inductively coupled plasma mass spectrometric transient signal acquisition and analyte concentration calculation. *J. Anal. At. Spectrom.* **11**, 899–904 (1996).
77. Stoll, H. M., Müller, W. & Prieto, M. I-STAL, a model for interpretation of Mg/Ca, Sr/Ca and Ba/Ca variations in speleothems and its forward and inverse application on seasonal to millennial scales. *Geochem., Geophys., Geosyst.* **13**, Q09004 (2012).
78. Paton, C., Hellstrom, J., Paul, B., Woodhead, J. & Hergt, J. Iolite: freeware for the visualisation and processing of mass spectrometric data. *J. Anal. At. Spectrom.* **26**, 2508–2518 (2011).
79. Lechleitner, F. A. et al. A novel approach for construction of radiocarbon-based chronologies for speleothems. *Quat. Geochronol.* **35**, 54–66 (2016).
80. Fohlmeister, J. & Lechleitner, F. A. STAlagmite dating by radiocarbon (star): a software tool for reliable and fast age depth modelling. *Quat. Geochronol.* **51**, 120–129 (2019).

81. Reimer, P. J. et al. IntCal13 and Marine13 radiocarbon age calibration curves 0–50,000 years cal BP. *Radiocarbon* **55**, 1896–1887 (2013).
82. Baskaran, M., Nix, J., Kuyper, C. & Karunakara, N. Problems with the dating of sediment core using excess ^{210}Pb in a freshwater system impacted by large scale watershed changes. *J. Environ. Radioact.* **138**, 355–363 (2014).
83. Francois, R., Bacon, M. P. & Suman, D. O. Thorium 230 profiling in deep-sea sediments: high-resolution records of flux and dissolution of carbonate in the equatorial Atlantic during the last 24,000 years. *Paleoceanography* **5**, 761–787 (1990).
84. Fohlmeister, J. et al. Winter precipitation changes during the Medieval Climate Anomaly and the Little Ice Age in arid Central Asia. *Quat. Sci. Rev.* **178**, 24–36 (2017).
85. Hua, Q., et al. Radiocarbon dating of a speleothem record of paleoclimate for Angkor, Cambodia. *Radiocarbon* **59**, 1873–1890 (2017).
86. Breitenbach, S. F. M. et al. COConstructing proxy records from age models (COPRA). *Clim. Past* **8**, 1765–1779 (2012).
87. Forman, E. C. G. et al. Data for “The Gulf Stream moved northward at the end of the Little Ice Age”. *Zenodo*, <https://doi.org/10.5281/zenodo.15477169> (2025).
88. Little, C. M. et al. The relationship between US East Coast sea level and the Atlantic Meridional Overturning Circulation: a review. *J. Geophys. Res.: Oceans* **124**, 6435–6458 (2019).
89. Aldhaif, A. M. et al. An aerosol climatology and implications for clouds at a remote marine site: case study over Bermuda. *J. Geophys. Res.: Atmos.* **126**, e2020JD034038 (2021).
90. Copernicus Marine Service. *ODYSEA Global S Surface Temperature Gridded Level 4 Daily Multi-Sensor Observations*. <https://doi.org/10.48670/mds-00321> (2024).

Acknowledgements

We thank the Bermuda Department of Conservation Services for a collecting permit for the speleothem. We thank A. Outerbridge for permission to enter Leamington Cave and G. Nolan for assistance with the cave monitoring equipment. We thank S.F.M. Breitenbach for assisting with the age model development and use of the COPRA algorithm. We also thank P. Moffa-Sánchez for the insightful comments and suggestions regarding the interpretation of our record. A European Research Council grant (ERC240167; J.U.L.B.) supported this work. Open access publication costs are supported by Durham University, Open Access Fund.

Author contributions

E.C.G.F. wrote the original draft, conducted the layer counts, carried out the data analysis, interpreted the results, and reviewed and edited the manuscript. J.U.L.B. wrote the original draft, conducted the layer counts, carried out the data analysis, interpreted the results, and reviewed and edited the manuscript. R.A.J. performed the trace element analysis, conducted the layer counts, and reviewed and edited the manuscript. F.A.L.

collected the sample, contributed to the construction of the radiocarbon chronology, and reviewed and edited the manuscript. I.W.W. collected the sample and contributed to the construction of the radiocarbon chronology. D.C.N. carried out the uranium-series dating. S.R.S. collected the sample and reviewed and edited the manuscript. D.A.R. carried out the uranium-series dating and reviewed and edited the manuscript. L.M.B. reviewed and edited the manuscript. C.M. contributed to the construction of the radiocarbon chronology. W.M. performed the trace element analysis and reviewed and edited the manuscript. A.J.P. collected and supplied the rainwater analysis data. All authors contributed to the project, discussed manuscript ideas, and approved the final manuscript.

Competing interests

The authors declare no competing interests.

Additional information

Supplementary information The online version contains supplementary material available at <https://doi.org/10.1038/s43247-025-02446-3>.

Correspondence and requests for materials should be addressed to Edward C. G. Forman.

Peer review information *Communications Earth & Environment* thanks the anonymous reviewers for their contribution to the peer review of this work. Primary Handling Editors: Yama Dixit and Aliénor Lavergne. A peer review file is available.

Reprints and permissions information is available at <http://www.nature.com/reprints>

Publisher's note Springer Nature remains neutral with regard to jurisdictional claims in published maps and institutional affiliations.

Open Access This article is licensed under a Creative Commons Attribution 4.0 International License, which permits use, sharing, adaptation, distribution and reproduction in any medium or format, as long as you give appropriate credit to the original author(s) and the source, provide a link to the Creative Commons licence, and indicate if changes were made. The images or other third party material in this article are included in the article's Creative Commons licence, unless indicated otherwise in a credit line to the material. If material is not included in the article's Creative Commons licence and your intended use is not permitted by statutory regulation or exceeds the permitted use, you will need to obtain permission directly from the copyright holder. To view a copy of this licence, visit <http://creativecommons.org/licenses/by/4.0/>.

© The Author(s) 2025